



Spatially resolved diffuse reflectance spectroscopy endoscopic sensing with custom Si photodetectors

BEN LARIVIERE,^{1,*} KATHERINE S. GARMAN,² N. LYNN FERGUSON,³
DEBORAH A. FISHER,² AND NAN M. JOKERST¹

¹Department of Electrical and Computer Engineering, Duke University, 101 Science Drive, Durham, NC 27708, USA

²Duke University Department of Medicine, Durham, NC 27710, USA

³Duke University Department of Pathology, Durham, NC 27710, USA

*benjamin.lariviere@duke.edu

Abstract: Early detection and surveillance of disease progression in epithelial tissue is key to improving long term patient outcomes for colon and esophageal cancers, which account for nearly a quarter of cancer related mortalities worldwide. Spatially resolved diffuse reflectance spectroscopy (SRDRS) is a non-invasive optical technique to sense biological changes at the cellular and sub-cellular level that occur when normal tissue becomes diseased, and has the potential to significantly improve the current standard of care for endoscopic gastrointestinal (GI) screening. Herein the design, fabrication, and characterization of the first custom SRDRS device to enable endoscopic SRDRS GI tissue characterization using a custom silicon (Si) thin film multi-pixel endoscopic optical sensor (MEOS) is described.

© 2018 Optical Society of America under the terms of the [OSA Open Access Publishing Agreement](#)

OCIS codes: (040.5160) Photodetectors; (170.6510) Spectroscopy, tissue diagnostics; (170.6935) Tissue characterization.

References and links

1. M. F. Byrne, N. Shahidi, and D. K. Rex, "Will computer-aided detection and diagnosis revolutionize colonoscopy?" *Gastroenterology* **153**(6), 1460–1464 (2017).
2. I. J. Bigio and J. R. Mourant, "Optical biopsy," *Encycl. Opt. Eng.* **1577**, 1593 (2003).
3. T. D. Wang and J. Van Dam, "Optical biopsy: A new frontier in endoscopic detection and diagnosis," *Clin. Gastroenterol. Hepatol.* **2**(9), 744–753 (2004).
4. E. Rodriguez-Diaz, Q. Huang, S. R. Cerda, M. J. O'Brien, I. J. Bigio, and S. K. Singh, "Endoscopic histological assessment of colonic polyps by using elastic scattering spectroscopy," *Gastrointest. Endosc.* **81**(3), 539–547 (2015).
5. Y. Zhu, N. G. Terry, J. T. Woosley, N. J. Shaheen, and A. Wax, "Design and validation of an angle-resolved low-coherence interferometry fiber probe for in vivo clinical measurements of depth-resolved nuclear morphology," *J. Biomed. Opt.* **16**(1), 011003 (2011).
6. G. J. Tearney, M. E. Brezinski, B. E. Bouma, S. A. Boppart, C. Pitris, J. F. Southern, and J. G. Fujimoto, "In vivo endoscopic optical biopsy with optical coherence tomography," *Science* **276**(5321), 2037–2039 (1997).
7. I. Georgakoudi, B. C. Jacobson, J. Van Dam, V. Backman, M. B. Wallace, M. G. Müller, Q. Zhang, K. Badizadegan, D. Sun, G. A. Thomas, L. T. Perelman, and M. S. Feld, "Fluorescence, reflectance, and light-scattering spectroscopy for evaluating dysplasia in patients with Barrett's esophagus," *Gastroenterology* **120**(7), 1620–1629 (2001).
8. G. Zonios, L. T. Perelman, V. Backman, R. Manoharan, M. Fitzmaurice, J. Van Dam, and M. S. Feld, "Diffuse reflectance spectroscopy of human adenomatous colon polyps in vivo," *Appl. Opt.* **38**(31), 6628–6637 (1999).
9. M. C. Skala, G. M. Palmer, K. M. Vrotsos, A. Gendron-Fitzpatrick, and N. Ramanujam, "Comparison of a physical model and principal component analysis for the diagnosis of epithelial neoplasias in vivo using diffuse reflectance spectroscopy," *Opt. Express* **15**(12), 7863–7875 (2007).
10. P. Thueler, I. Charvet, F. Bevilacqua, M. St Ghislain, G. Ory, P. Marquet, P. Meda, B. Vermeulen, and C. Depeursinge, "In vivo endoscopic tissue diagnostics based on spectroscopic absorption, scattering, and phase function properties," *J. Biomed. Opt.* **8**(3), 495–503 (2003).
11. Z. Ge, K. T. Schomacker, and N. S. Nishioka, "Identification of colonic dysplasia and neoplasia by diffuse reflectance spectroscopy and pattern recognition techniques," *Appl. Spectrosc.* **52**(6), 833–839 (1998).
12. D. A. Boas, C. Pitris, and N. Ramanujam, "Handbook of Biomedical Optics," in *Handbook of Biomedical Optics* (CRC press, 2016), p. Chap 6.

13. J. Y. Lo, B. Yu, H. L. Fu, J. E. Bender, G. M. Palmer, T. F. Kuech, and N. Ramanujam, "A strategy for quantitative spectral imaging of tissue absorption and scattering using light emitting diodes and photodiodes," *Opt. Express* **17**(3), 1372–1384 (2009).
14. E. Rodriguez-Diaz, I. J. Bigio, and S. K. Singh, "Integrated optical tools for minimally invasive diagnosis and treatment at gastrointestinal endoscopy," *Robot. Comput.-Integr. Manuf.* **27**(2), 249–256 (2011).
15. T. Papaioannou, N. W. Preyer, Q. Fang, A. Brightwell, M. Carnohan, G. Cottone, R. Ross, L. R. Jones, and L. Marcu, "Effects of fiber-optic probe design and probe-to-target distance on diffuse reflectance measurements of turbid media: an experimental and computational study at 337 nm," *Appl. Opt.* **43**(14), 2846–2860 (2004).
16. B. Yu, H. L. Fu, and N. Ramanujam, "Instrument independent diffuse reflectance spectroscopy," *J. Biomed. Opt.* **16**(1), 011010 (2011).
17. J. S. Dam, C. B. Pedersen, T. Dalgaard, P. E. Fabricius, P. Aruna, and S. Andersson-Engels, "Fiber-optic probe for noninvasive real-time determination of tissue optical properties at multiple wavelengths," *Appl. Opt.* **40**(7), 1155–1164 (2001).
18. T. J. Farrell, B. C. Wilson, and M. S. Patterson, "The use of a neural network to determine tissue optical properties from spatially resolved diffuse reflectance measurements," *Phys. Med. Biol.* **37**(12), 2281–2286 (1992).
19. A. Kienle, L. Lilge, M. S. Patterson, R. Hibst, R. Steiner, and B. C. Wilson, "Spatially resolved absolute diffuse reflectance measurements for noninvasive determination of the optical scattering and absorption coefficients of biological tissue," *Appl. Opt.* **35**(13), 2304–2314 (1996).
20. K.-B. Sung, K.-W. Shih, F.-W. Hsu, H.-P. Hsieh, M.-J. Chuang, Y.-H. Hsiao, Y.-H. Su, and G.-H. Tien, "Accurate extraction of optical properties and top layer thickness of two-layered mucosal tissue phantoms from spatially resolved reflectance spectra," *J. Biomed. Opt.* **19**(7), 77002 (2014).
21. O. Senlik, G. Greening, T. J. Muldoon, and N. M. Jokerst, "Spatially resolved diffuse reflectance spectroscopy of two-layer turbid media using a densely packed multi-pixel photodiode probe," *Proc. SPIE* **9700**, 97000O (2016).
22. G. J. Greening, H. M. James, M. K. Dierks, N. Vongkittiangorn, S. M. Osterholm, N. Rajaram, and T. J. Muldoon, "Towards monitoring dysplastic progression in the oral cavity using a hybrid fiber-bundle imaging and spectroscopy probe," *Sci. Rep.* **6**(1), 26734 (2016).
23. D. J. Cappon, T. J. Farrell, Q. Fang, and J. E. Hayward, "Fiber-optic probe design and optical property recovery algorithm for optical biopsy of brain tissue," *J. Biomed. Opt.* **18**(10), 107004 (2013).
24. R. Hennessy, W. Goth, M. Sharma, M. K. Markey, and J. W. Tunnell, "Effect of probe geometry and optical properties on the sampling depth for diffuse reflectance spectroscopy," *J. Biomed. Opt.* **19**(10), 107002 (2014).
25. "Thorlab's Fiber Probes," https://www.thorlabs.com/newgrouppage9.cfm?objectgroup_id=7794.
26. I. J. Bigio and S. Fantini, *Quantitative Biomedical Optics: Theory, Methods, and Applications* (Cambridge University Press, 2016).
27. D. K. Rex, C. Kahi, M. O'Brien, T. R. Levin, H. Pohl, A. Rastogi, L. Burgart, T. Imperiale, U. Ladabaum, J. Cohen, and D. A. Lieberman, "The American Society for Gastrointestinal Endoscopy PIVI (Preservation and Incorporation of Valuable Endoscopic Innovations) on real-time endoscopic assessment of the histology of diminutive colorectal polyps," *Gastrointest. Endosc.* **73**(3), 419–422 (2011).
28. H.-W. Wang, J.-K. Jiang, C.-H. Lin, J.-K. Lin, G.-J. Huang, and J.-S. Yu, "Diffuse reflectance spectroscopy detects increased hemoglobin concentration and decreased oxygenation during colon carcinogenesis from normal to malignant tumors," *Opt. Express* **17**(4), 2805–2817 (2009).
29. N. Rajaram, A. Gopal, X. Zhang, and J. W. Tunnell, "Experimental validation of the effects of microvasculature pigment packaging on in vivo diffuse reflectance spectroscopy," *Lasers Surg. Med.* **42**(7), 680–688 (2010).
30. C. Zhu, G. M. Palmer, T. M. Breslin, J. Harter, and N. Ramanujam, "Diagnosis of breast cancer using diffuse reflectance spectroscopy: Comparison of a Monte Carlo versus partial least squares analysis based feature extraction technique," *Lasers Surg. Med.* **38**(7), 714–724 (2006).
31. A. Dhar, K. S. Johnson, M. R. Novelli, S. G. Bown, I. J. Bigio, L. B. Lovat, and S. L. Bloom, "Elastic scattering spectroscopy for the diagnosis of colonic lesions: Initial results of a novel optical biopsy technique," *Gastrointest. Endosc.* **63**(2), 257–261 (2006).
32. C. Zhu, G. M. Palmer, T. M. Breslin, F. Xu, and N. Ramanujam, "Use of a multiseparation fiber optic probe for the optical diagnosis of breast cancer," *J. Biomed. Opt.* **10**(2), 024032 (2005).
33. S. Dhar, J. Lo, B. Yu, M. A. Brooke, N. Ramanujam, and N. M. Jokerst, "Custom annular photodetector arrays for breast cancer margin assessment using diffuse reflectance spectroscopy," in *Biomedical Circuits and Systems Conference (BioCAS), 2011 IEEE* (IEEE, 2011), pp. 440–443.
34. S. Dhar, D. M. Miller, and N. M. Jokerst, "High responsivity, low dark current, heterogeneously integrated thin film Si photodetectors on rigid and flexible substrates," *Opt. Express* **22**(5), 5052–5059 (2014).
35. D. M. Miller and N. M. Jokerst, "Flexible silicon sensors for diffuse reflectance spectroscopy of tissue," *Biomed. Opt. Express* **8**(3), 1512–1524 (2017).
36. D. S. Ferreira, V. C. Pinto, J. H. Correia, and G. Minas, "Spectroscopic Detection of Gastrointestinal Dysplasia Using Optical Microsensors," *IEEE Trans. Biomed. Eng.* **58**(9), 2633–2639 (2011).
37. S. Pimenta, E. M. S. Castanheira, and G. Minas, "Optical Microsystem for Analysis of Diffuse Reflectance and Fluorescence Signals Applied to Early Gastrointestinal Cancer Detection," *Sensors (Basel)* **15**(12), 3138–3153 (2015).
38. O. Senlik and N. M. Jokerst, "Concentric Multipixel Silicon Photodiode Array Probes for Spatially Resolved

- Diffuse Reflectance Spectroscopy,” *IEEE J. Sel. Top. Quantum Electron.* **22**(3), 7–12 (2016).
39. G. I. Zonios, R. M. Cothren, J. T. Arendt, J. Wu, J. VanDam, J. M. Crawford, R. Manoharan, and M. S. Feld, “Morphological model of human colon tissue fluorescence (vol 43, pg 113, 1996),” *IEEE Trans. Biomed. Eng.* **43**, 437 (1996).
 40. T. RadianT Zemax LLC, Zemax 12 EE OpticStudio, www.zemax.com
 41. O. Senlik, Duke University ECE Dept, 100 Science Dr., Durham, NC, 27708. “Personal Communication,” (2015).
 42. T. M. Bydlon, S. A. Kennedy, L. M. Richards, J. Q. Brown, B. Yu, M. K. Junker, J. Gallagher, J. Geradts, L. G. Wilke, and N. Ramanujam, “Performance metrics of an optical spectral imaging system for intra-operative assessment of breast tumor margins,” *Opt. Express* **18**(8), 8058–8076 (2010).
 43. S. Dhar, “Development of Custom Imaging Arrays for Biomedical Spectral Imaging Systems,” Duke PhD Diss. (2012).
 44. O. Senlik, “Custom Photodiode Arrays for Diffuse Reflectance Spectroscopic Imaging of Tissues,” Duke PhD Diss. (2016).
 45. S. L. Jacques, “Optical properties of biological tissues: a review,” *Phys. Med. Biol.* **58**(11), R37–R61 (2013).
 46. C. Mätzler, “MATLAB functions for Mie scattering and absorption, version 2,” IAP Res. Report **8** (2002).
 47. G. M. Palmer and N. Ramanujam, “Monte Carlo-based inverse model for calculating tissue optical properties. Part I: Theory and validation on synthetic phantoms,” *Appl. Opt.* **45**(5), 1062–1071 (2006).
 48. L. R. Jones, N. W. Preyer, H. C. Wolfson, D. M. Reynolds, M. A. Davis, and M. B. Wallace, “Monte Carlo model of stricture formation in photodynamic therapy of normal pig esophagus,” *Photochem. Photobiol.* **85**(1), 341–346 (2009).

1. Introduction

Endoscopic screening and surveillance of dysplasia (abnormal cells that can progress to cancer) and malignancy (cancer) in the colon and esophagus are currently performed using white light endoscopy (WLE), which allows physicians to inspect the mucosal surface of gastrointestinal (GI) tissues with video imaging. During WLE, physicians survey the epithelial surface of the esophagus or colon in search of dysplastic, malignant, or other high-risk tissues. In conditions such as Barrett’s esophagus (intestinal metaplasia of the esophagus), epithelial tissue is known to be of elevated risk of dysplasia, but dysplastic lesions are not identifiable with WLE. As a result, physicians typically randomly sample tissue from the at-risk area. Other limitations of WLE include difficulty in assessing sidewall lesions, removal of non-neoplastic tissue, incomplete resection of abnormal tissues because the borders of the normal versus abnormal tissue cannot be determined, and missed detection of abnormal tissues (which should be biopsied) because they are difficult to detect with WLE. If the structural and biochemical indicators of disease that are present within these tissues could be readily detected during endoscopy, these indicators could improve diagnostic accuracy and guide biopsy locations [1].

Noninvasive optical technologies to enhance WLE can be broadly classified as imaging or spectroscopic [2–7]. Imaging technologies such as optical coherence tomography, narrowband imaging, and confocal endomicroscopy complement WLE with images that are interpreted similarly to histopathologic cross sections [5,7]. In contrast, spectroscopic techniques can classify tissues (e.g. neoplastic or non-neoplastic) through quantitative measurements of tissue chemistry and structure [5,7–10], or through spectral pattern recognition algorithms [4,9,11], often in real-time.

Investigations of spectroscopy for endoscopic in-vivo colon and esophageal characterization include diffuse reflectance spectroscopy (DRS), low-coherence enhanced backscatter spectroscopy (LEBS), angle-resolved low-coherence interferometry (a-LCI), Raman spectroscopy, and intrinsic fluorescence spectroscopy (IFS). Of these approaches, DRS has the advantage of simple, scalable, compact instrumentation with demonstrated high accuracy characterization of both the optical absorption and the scattering properties of tissue. Other techniques are primarily sensitive to either scattering (a-LCI [5]), which characterizes tissue, or to absorption (Raman, IFS [12]), which reveals tissue biochemistry [3], or contain complex optical components that are difficult to miniaturize [13].

A wide variety of DRS probes have been investigated for tissue spectroscopy, with the probes for endoscopic GI characterization reported to date consisting of small optical fiber

bundles with a single illumination fiber and one or more collection fibers [14–17]. The typical single illumination/detection separation of the fibers does not provide spatial resolution. Thus, the spectra collected by each probe are analyzed solely as a function of wavelength. In contrast, an approach that increases the dimensionality of the DRS data is spatially resolved DRS (SRDRS). SRDRS uses multiple light collection locations with varied illumination/detection separations, enabling depth sensitivity since photons collected farther from the illumination location have, on average, traveled more deeply into the tissue.

The utility of SRDRS for quantitative optical characterization of tissues has been widely recognized [18–22]. The increased dimensionality of the DRS data yields increased information density for the unique determination of tissue optical properties, and the illumination/detection separations of SRDRS probes may be optimized for specific tissue applications to reduce noise and target specific interrogation depths [23,24]. These advantages have motivated several investigations into the endoscopic implementation of SRDRS for characterization of GI screening for dysplasia and cancer using fiber bundle probes for in-vivo characterization of stomach tissues [10], colon tissues [11], and oral tissues [22]. However, fiber bundle probes have several disadvantages for SRDRS, including low collection efficiency due to low numerical aperture (NA), low fill factor, and limited geometrical collection configurations (typically round) [25, 26].

These limitations of fiber SRDRS probes can be addressed by using photodetectors (PDs) for collection instead of fibers since PDs have higher numerical apertures and larger fill factors than fibers, and custom PDs can be fabricated in any shape. Commercially available PDs are limited to specific sizes and geometries, and are difficult to pack closely. In contrast, the design and implementation of PDs that are customized for a specific tissue and application can take full advantage of optimized geometry and fill factors. The work reported herein describes the first use of an array of custom Si PDs for a SRDRS endoscopic probe. This custom Si multispectral endoscopic optical sensor (MEOS) SRDRS probe utilizes multiple PDs in an array with illumination and collection distances and geometries optimized for GI epithelial tissue characterization. This approach leverages the high optical collection efficiency of Si PDs as well as the ability to optimize Si PD geometries and fill factors for a specific application. These advantages can yield improved performance over fiber based SRDRS systems, and have the potential to achieve the specificity and selectivity required for clinical adoption of DRS as a noninvasive enhancement of WLE [27].

2. Diffuse reflectance spectroscopy

DRS quantifies tissue structure and chemistry by measuring volume averaged optical properties, including the absorption coefficient (μ_a), scattering coefficient (μ_s), scattering anisotropy (g), and reduced scattering coefficient ($\mu'_s = \mu_s \times (1 - g)$). DRS instrumentation consists of light delivery to a tissue, and detection of a fraction of the reflected light from the tissue after the light has propagated and scattered within the tissue. Light scattering within tissues arises due to the refractive index difference at the interface between structures such as collagen, mitochondria, and nuclei, which have a higher refractive index than their surrounding intracellular fluid [26]. Absorption in tissues occurs when a molecule is excited by an incident photon. Scattering and absorption tissue optical properties can be used to characterize tissue parameters such as hemoglobin concentration, oxygen saturation, blood volume fraction, and beta-carotene concentration [28–30], and to classify dysplasia and cancer [11,31,32].

The performance, size, and cost of DRS and SRDRS systems can be improved by replacing optical fibers used for reflectance collection with custom Si PDs. Fiber-based light collection limits the probe reflectance collection efficiency both because the cylindrical fiber cores are surrounded by noncollecting fiber cladding layers, which limits the photon collection fill factor, and because the low NA of fiber probes (typical fiber NA = 0.22

[25,26]) limits the acceptance angle of the reflected photons. Replacing collection fibers with high NA Si PDs (typical NA > 0.95 [13]) improves the reflectance collection efficiency [31], which in turn improves system signal to noise ratio (SNR) [13]. Reported research on replacing DRS collection fibers with annular Si PDs produced a DRS SNR and spectral response that were better than a comparable fiber based system [33]. Si PDs can be implemented in many formats: high responsivity, low dark current single crystal Si PDs have been reported in thin film form, fabricated by bonding 10 μm thick Si PDs to flexible and transparent substrates [34], enabling bendable, conforming tissue reflectance spectroscopy probes [35]. The use of silicon (Si) photodetectors (PDs) with integrated surface optical filters has also been explored, but these devices were implemented with single illumination/detection separations for each wavelength of interest [36,37]. For SRDRS, Si probes sensitive to photon path length were demonstrated by developing a custom Si PD probe consisting of 24 concentric semi-annular PDs, providing 24 distinct source to detection spacings with a single illumination aperture [38]. SRDRS probes can be optimized for a given application by modeling and engineering design if the relevant range of tissue optical properties is known. Prior work has demonstrated the benefits of optimizing illumination/collection distances as well as fiber diameters in fiber-based SRDRS probes [23,24]. This paper describes the first SRDRS probe that utilizes the fully customizable geometry of Si PDs to optimize a probe for a specific targeted SRDRS tissue application. The MEOS SRDRS probe described herein is also the first Si PD SRDRS probe optimized in an endoscopic tissue spectroscopy format, and the first implemented in thin film Si.

The MEOS prototype is an SRDRS probe comprised of an array of three custom concentric semi-annular thin film Si PDs that are consistent in total size with implementation in an endoscopic working channel (2.4 mm in diameter). The Si PDs face the tissue to be measured, as shown in Fig. 1, which is a conceptual diagram of the MEOS prototype. Photons are incident via a fiber from the back of the PD array, and pass through a hole in the center of the PD array to illuminate the tissue. In the tissue, the photons experience scattering and absorption, and the reflected photons that interrogate the tissue are collected and detected by the MEOS PDs when they exit the tissue. The number and geometry of the MEOS detectors were chosen to provide spatial resolution while maintaining a compact overall size and high SNR at each PD. The prototype device reported herein interrogates a tissue surface area of approximately 4.5 mm^2 and a depth of approximately 0.5-2 mm (depending upon the wavelength), as illustrated by the colored bands representing the photon paths in Fig. 1. The potential for low cost, scalable manufacture of these probes is excellent since standard Si PD manufacturing processes were used to fabricate the probes and these Si PDs can also be integrated onto flexible or conformal substrates [34,35].

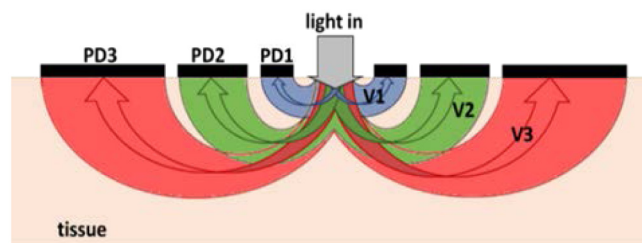


Fig. 1. Cross-sectional conceptual diagram of the measurement of multiple partially overlapping tissue volumes V1, V2 and V3 by three photodiodes PD1, PD2 and PD3.

3. Probe design, fabrication, and device characterization

3.1. Design modeling and design criteria

To optimize the Si PD geometries for a specific application, the prototype MEOS device design began with 3D Monte Carlo (MC) modeling to maximize the contrast between the

reflectance from human colon adenomatous tissue (a form of dysplasia) and normal colon epithelial tissue. Adenomatous tissue Reported optical properties (μ'_s and μ_a) for human colon tissue in the visible spectrum from 415 nm to 650 nm [39] were used as inputs to a MC model implemented in Zemax [40]. The MEOS probe diameter was limited to 2.4 mm for implementation in the instrument channel of commercial endoscopes. The MEOS probe design aimed to satisfy three criteria: (1) minimum photocurrent from each PD of 80 pA for the most attenuating phantom, (2) minimum SNR of 40 dB for each PD, and (3) high contrast between the two classes of tissue.

The first criterion ensured that every PD was able to measure high absorbance tissue (producing low PD current) with a minimum signal current of 80 pA designed to exceed the estimated dark current. The dark current design estimate was based upon dark current densities of reported thin film Si PDs [36]. This criterion produced a tradeoff between the widths of the three PDs. As the size of PD1 increased, the photocurrent available to PD2 and PD3 decreased due to decreased area as well as increased distance of PD2 and PD3 from the illumination source (increasing distance from the illumination source results in fewer reflected photons). In the modeling, the largest PD1 that enabled PD2 and PD3 to realize the 80 pA minimum current was a PD1 with width of 58 μm , for which PD1 generated 86 pA of photocurrent in the most attenuating case. The black dashed contour lines on Fig. 2, below, shows the modeled minimum photocurrents on PD2 and PD3 for a 58 μm wide PD1 as functions of PD2 and PD3 widths, showing the widths could each be varied significantly while still maintaining photocurrents above 80 pA.

The minimum SNR criterion of 40 dB was chosen so that the MEOS SNR would be comparable to the SNR of previously reported DRS systems that have demonstrated high accuracy tissue optical property measurements [13,42]. This criterion was satisfied by computing the SNR for all 3 PDs across all simulated wavelengths for all combinations of PD2 widths between 50 and 150 μm and PD3 widths between 200 and 800 μm for a PD1 width fixed at 58 μm . Figure 2 shows the SNR contours as red dashed lines. The SNR decreases in magnitude with increasing PD2 and PD3 width because the dark current increases with PD area more quickly than the photocurrent increases. The dark current variance was estimated based on the dark current variance for comparable reported thin film Si PDs [34,41].

Criterion (3) aimed to realize high contrast between the simulated adenomatous tissue and the simulated normal tissue. Contrast between tissue types is defined as in Eq. (1) below,

$$\Gamma(\lambda, PD_i) = \left(1 - \frac{I_{adenoma}(\lambda, PD_i)}{I_{normal}(\lambda, PD_i)} \right) \quad (1)$$

where $I_{adenoma}(\lambda, PD_i)$ and $I_{normal}(\lambda, PD_i)$ are the MC modeled photocurrents from the adenomatous and normal tissues, respectively, as functions of wavelength and PD number. To facilitate analysis, a contrast function of merit (C_{FOM}) is defined in Eq. (2) below, which is the product of the contrast at each PD averaged across all wavelengths:

$$C_{FOM} = \Pi_{i=1}^3 \text{mean}_{\lambda}(\Gamma(\lambda, PD_i)) \quad (2)$$

Measurements and modeling of the maximum power throughput of the light source available for prototype testing informed the choice of a 750 μm diameter for the illumination aperture to ensure sufficient optical throughput. A 40 μm offset of the inner PD (PD1) from the aperture was used to avoid excessive PD current due to back illumination of the inner PD from the fiber [43,44], and a 9 μm separation between each PD was added for electrical isolation. Figure 2 displays the variation in C_{FOM} as a function of varying PD2 and PD3 width. The magenta circle denotes the geometry that co-optimizes all three criteria; namely, that all three PDs have minimum photocurrents (in highly absorbing phantoms) of greater

than 80 pA, the SNR for each PD is greater than 40 dB for all wavelengths, and the system maximizes the contrast figure of merit. The resulting widths of the three detectors are 58 μm , 100 μm , and 550 μm for PD1, PD2, and PD3, respectively, with center to center source-detector separations of 444 μm , 53 μm , and 866 μm . Thus, the MC-based design of the MEOS probe was complete.

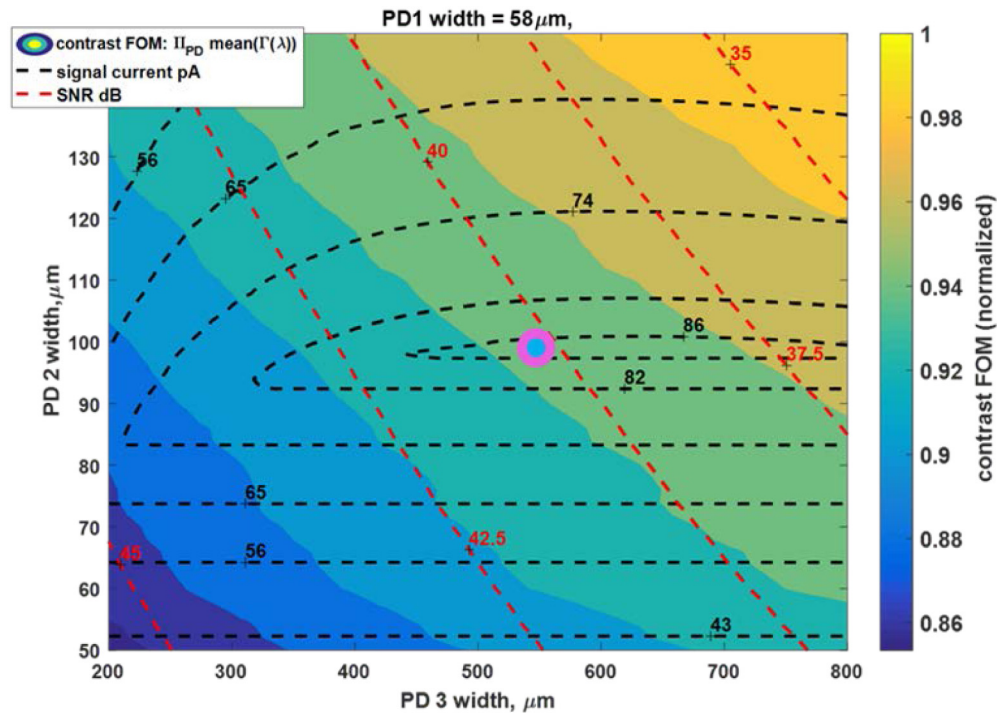


Fig. 2. Dependence of the minimum SNR, contrast FOM, and the minimum signal contours as functions of PD2 and PD3 width for PD1 width fixed at 58 μm . The magenta circle in the center of the plot denotes the PD2 and PD3 widths of 100 μm , and 550 μm , respectively, which satisfy the design criteria.

3.2. Device fabrication and device characterization

Fabrication and packaging of the custom Si MEOS prototype used standard semiconductor manufacturing processes. Fabrication began with p-type Si-on-insulator (SOI) wafers with a 10 μm thick device layer. Concentric n-wells were diffused into the p-type SOI device layer using a spin-on phosphorus dopant and high temperature annealing, forming arrays of PN junction diode PDs. The n-type contact was electron beam vacuum deposited Ti (50 nm)/Ni (50 nm)/Au (250 nm). The Si PD mesas were then defined using a plasma etch (22% C_4F_8 , 73% SF_6 , and 5% O_2), and the structure was bonded to a temporary carrier substrate. The Si handle wafer was removed using a plasma etch (90% SF_6 and 10% O_2), followed by selective removal of the SOI oxide layer with a buffered oxide wet etch, resulting in 10 μm thick Si PDs. After an Al (50 nm)/Ti (50 nm)/Ni (50 nm)/Au (250 nm) p-type contact metallization, the PDs were bonded to a glass substrate with metallized Cr (50 nm)/Ti (200 nm)/Au (250 nm) bonding and electrical contacts. Gold to gold thermocompression bonding was used to mechanically adhere and electrically connect the thin film PDs to the metallized host glass substrate. Finally, an antireflective (AR) coating of 60 nm of silicon nitride was deposited onto the PDs, and the devices were packaged onto a printed circuit board. The AR coating also functioned as a passivation layer for the Si surfaces, reducing the recombination velocity

of electrons at the PD surface and thereby reducing the dark current [33]. A photomicrograph of the fabricated three PD MEOS probe is shown in Fig. 3(a).

The performance of the MEOS prototype was characterized by measuring the responsivity and dark current of each of the PDs. Currents were measured with a Keithley 4200 source measurement unit, with surface normal illumination provided by a 1 mm diameter optical fiber with a 0.39 NA coupled to a Xenon lamp through a Newport CS130 monochromator and focused onto the PD surfaces through an objective lens. Wavelengths ranging from 450 nm to 650 nm in increments of 10 nm were incident upon the PDs. The responsivity and dark current for each PD was measured at zero voltage bias, the MEOS operating point during SRDRS measurements. The dark current densities ranged from 13 pA/mm² to 48 pA/mm², with the magnitudes of the dark currents ranging from 14 pA for PD1 to 69 pA for PD3. The responsivities for the fabricated PDs ranged from 0.13 A/W at 450 nm to 0.41 A/W at 650 nm, as shown in Fig. 3(b), which is comparable to reported thin film Si PDs [34].

Liquid phantoms were used to characterize the MEOS SRDRS performance, and the illumination for these experiments was delivered by the same 1 mm diameter fiber used for the responsivity characterization. The fiber output was coupled to the back of the transparent MEOS substrate and aligned through the glass substrate to the 750 μ m diameter aperture in the back of the PD array to illuminate the tissue through the aperture (hole) in the PD array. Light incident on the backside of the thin film device outside of the aperture region was blocked by a 500 nm layer Cr/Ti/Au coating on the glass substrate. Once aligned, the fiber and the MEOS prototype were both secured to an optical mount, preventing variation in optical coupling during testing. The typical optical power incident on the phantom or tissue through the PD aperture ranged from 16 μ W at 450 nm to 8 μ W at 650 nm, which was dictated by the Xenon lamp power output spectrum and the experimental apparatus.

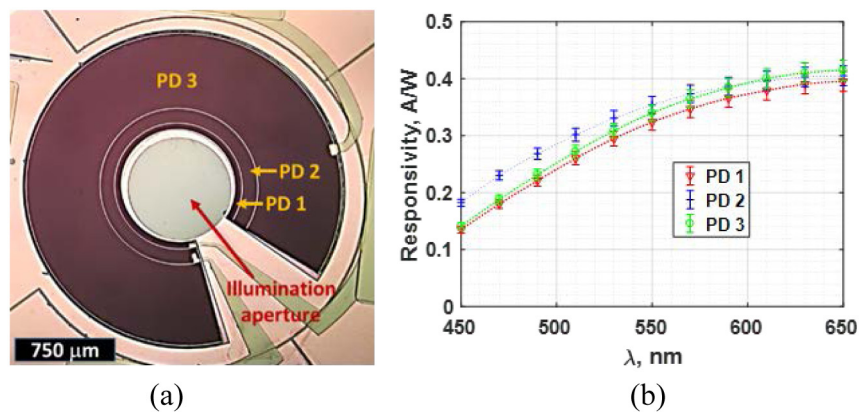


Fig. 3. (a) Photomicrograph of the front (tissue facing) side of a fabricated MEOS three PD probe. The scale bar shown is 750 μ m, which is also the diameter of the illumination aperture. (b) Surface normal responsivity for a fabricated MEOS probe, with error bars as indicated.

4. Experimental phantom testing and probe model validation

4.1. Tissue phantom preparation and experimental measurement

To assess the performance of the fabricated MEOS prototype, reflectance measurements were performed on liquid phantoms with well-defined optical properties. Phantoms were prepared with 1 μ m diameter polystyrene spheres (Polysciences, Inc.) as the scattering agent, powdered hemoglobin (Sigma-Aldrich Co. LLC.) as the absorbing agent, and de-ionized (DI) water as the solvent. A total of six turbid hemoglobin-containing phantoms were prepared, with sphere and hemoglobin concentrations chosen such that the scattering and absorption coefficients of the liquid phantoms were consistent with the reported values of absorption and scattering for

normal and adenomatous colon polyps used in the MC forward model which informed the probe design. The anisotropy factor of the polystyrene spheres was 0.92 across the wavelengths measured, and does not depend on sphere concentration, and appropriate for the reported value of 0.9 for colon tissue [45]. Optical absorption coefficients for the prepared phantoms were calculated by measuring the extinction coefficient for the hemoglobin powder dissolved in DI water, while the scattering coefficients and anisotropy were calculated using Mie theory [46]. The scattering coefficients (μ_s) ranged from 40.1 cm^{-1} to 101.6 cm^{-1} , and the absorption coefficients (μ_a) ranged from 0.25 cm^{-1} to 16.25 cm^{-1} . Figure 4 displays the experimental phantom optical properties. Phantom 1 has absorption coefficients shown in red, and Phantoms 2-6 have absorption coefficients shown in blue, representing normal tissue.

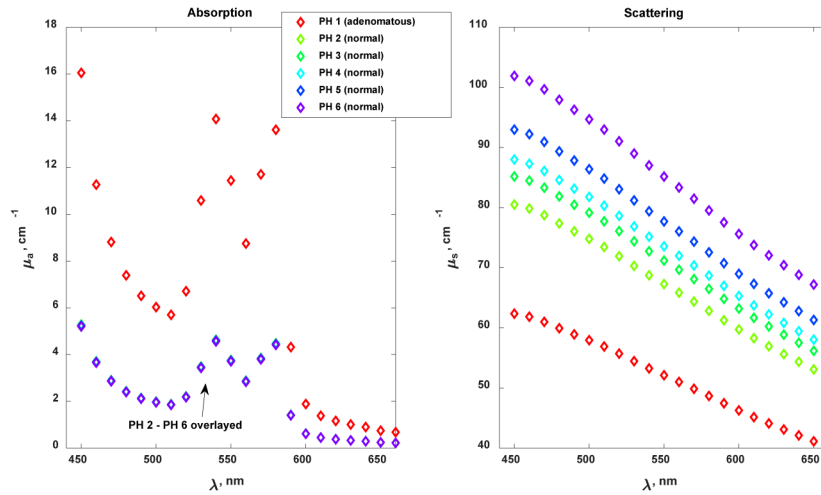


Fig. 4. Scattering and absorption coefficients for each of the prepared liquid phantoms. The inset legend applies to both graphs. On the left-hand graph, Phantom 1 has absorption coefficients shown in red, and Phantoms 2-6 have absorption coefficients shown in blue.

Phantoms were measured with the MEOS probe surface placed into the liquid phantom solution such that the entire front face of each PD in the array was immersed. Before and between each phantom measurement, the MEOS surface was cleaned by a de-ionized water rise and dry nitrogen and a reference measurement was performed with a 99% diffuse reflectance standard (Labsphere, Inc. SRS-99-010). The reference standard measurements were used to remove the Xenon lamp spectrum from the DRS data, and to validate system stability throughout the experiments. Before and after phantom measurements, the background currents were measured as a function of wavelength with the detector array directed toward a zero-reflectance background. Background currents were primarily due to small amounts of PD back illumination, and averaged less than 2% of the phantom photocurrent. The diffuse reflectance per unit area of the PD (A_{PD}) is $R(\lambda)$:

$$R(\lambda) = \left(\frac{I_{phantom}(\lambda) - I_{background}(\lambda)}{I_{standard}(\lambda) - I_{background}(\lambda)} \right) / A_{PD} \quad (3)$$

where $I_{phantom}(\lambda)$, $I_{standard}(\lambda)$, and $I_{background}(\lambda)$ are the wavelength dependent currents produced by the PD due to phantom and diffuse standard reflectance, and the background current, respectively.

A forward MC model of the probe was developed to compare to the experimental measurements. Since the reflectance described by Eq. (3) is a relative reflectance value, while

MC simulations produce absolute reflectance values, to compare the phantom reflectance measured experimentally to MC simulations, an additional scattering-only solution of polystyrene beads was measured. By MC simulating the reflectance of the scattering-only solution and dividing the simulated tissue phantom reflectance by the simulated reference phantom reflectance, equivalent relative reflectance values were obtained for comparative purposes [47]. To obtain $R_{scaled}(\lambda)$, each measured phantom reflectance was divided by the measured reflectance from the scattering-only solution, $R_{reference}(\lambda)$.

The comparison of the MC simulated and measured per-unit-area reflectance, $R_{scaled}(\lambda)$, for each of the PDs in the MEOS probe, for all six phantoms, are shown in Fig. 5. The measured and simulated data are in good agreement, with an average root-mean-square (RMS) error across all three PDs of 8.4% with a maximum RMS error of 9.2% on PD3. As expected, $R_{scaled}(\lambda)$ decreases exponentially with increasing detector radius for both the simulated and measured reflectance.

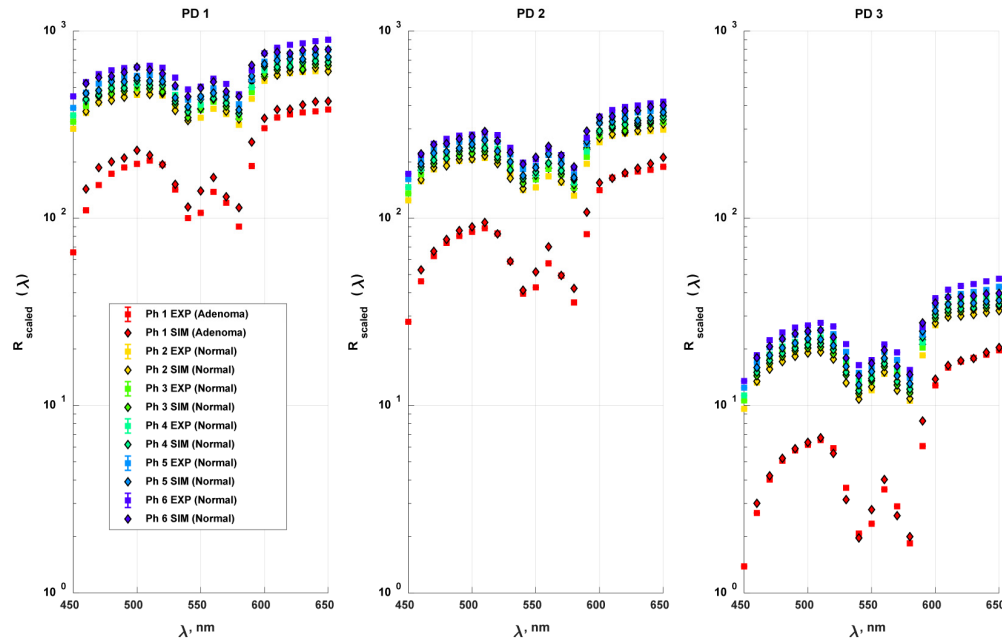


Fig. 5. Experimental and MC simulated scaled reflectance spectra from six liquid phantoms for each of the three MEOS PDs. From left to right, data and simulations for PD1 through PD3 are shown. Error bars are included in the plots, but are indistinguishable from the data points.

4.2. Signal to noise characterization

The signal to noise ratio is an important figure of merit for DRS and SRDRS systems for high accuracy tissue classification. The SNR was calculated for each of the six phantoms measured, with the SNR in dB defined as,

$$SNR = 20 \log_{10} \left(\frac{\overline{I_{phantom}} - \overline{I_{background}}}{\sigma_{phantom} + \sigma_{background}} \right) \quad (4)$$

where $\overline{I_{phantom}}$ and $\overline{I_{background}}$ are the phantom and background photocurrents averaged over 30 measurements at a 20 ms integration time per measurement, and $\sigma_{phantom}$ and $\sigma_{background}$ are the corresponding standard deviations of the phantom and background, respectively.

For the measured and simulated spectra displayed in Fig. 5, which spans the reported range of colon epithelial tissue optical properties [39], the SNR is above 40 dB for all wavelengths between 450 and 650 nm. The measured SNR ranges from a low of 40.8 dB on PD1 when measuring highly absorbing Phantom 1, to a high of 53 dB on PD3 while measuring Phantom 5, with an average of 46 dB across all phantom measurements. This range of SNR is comparable to or greater than SNR for previously reported DRS systems that achieved high accuracy tissue optical property extraction [13,42].

5. Porcine esophageal tissue SRDRS measurements, histology, and modeling

5.1. Porcine measurements

To evaluate the MEOS probe performance in a context more relevant to human gastrointestinal tissues, measurements on samples of freshly excised porcine esophageal tissues were performed. Esophageal tissues were obtained from City Packing (Burlington, NC), through a North Carolina Department of Agriculture permit, and measurements were performed within 12 hours of animal sacrifice. Tissue samples were stored in saline solution chilled with ice until the time of measurement. Samples of tissue to be measured were cut to approximately 1 cm x 1 cm and placed in direct contact with the probe, as shown below in a photograph of the probe and tissue experimental apparatus in Fig. 6.



Fig. 6. Photograph of a full-thickness porcine esophageal tissue sample in contact with the MEOS probe surface, which is completely covered by the tissue. An optical fiber used for light delivery is coupled to the backside of the MEOS glass substrate through a hole in the yellow printed circuit board shown in the photograph above.

Three distinct types of porcine esophageal tissue were harvested and measured: normal, irregularly keratinized, and with denuded epithelial tissue. Figure 7(a) shows the measured SRDRS spectra for the normal porcine esophageal epithelial tissue shown in Fig. 6. The reflectance spectra in Fig. 7 were calculated using Eq. (3), but are not scaled by PD area to facilitate comparison between PDs. The error bars on the data points are the standard deviation between 30 measurements taken at each wavelength, and the probe was completely removed then reapplied to the tissue every ten measurements to include the repeatability of measurements of a single tissue sample. In Fig. 7(b), min-max normalization was used to highlight differences in the features of the normal porcine data of Fig. 7(a). The min-max normalization subtracts the minimum reflectance value from all of the reflectance values before normalization for each PD, resulting in the normalized spectra spanning the full range from 0 to 1.

One feature of the min-max normalized spectra in Fig. 7(b) is the rise in the PD3 spectra on wavelengths longer than 560 nm compared to the same spectra from PD1 and PD2, which are nearly identical at these wavelengths. We hypothesize that this is due to the increased and deeper interrogated tissue volume of PD3, which reaches beyond the mucosa, into the submucosa, which has higher absorption coefficients [48]. Thus, for PD3, a larger fraction of the light collected has passed into the deeper, more perfused submucosal tissue, which results in higher hemoglobin absorption. This indicates that the MEOS probe can yield depth information about the tissue.

Secondly, the normal porcine tissue shown in Fig. 7(a) has significantly different reflectance compared to the denuded and irregularly keratinized tissues shown in Figs. 7(c) and 7(d), respectively. To enable a comparison between the reflectance measured from these three tissues, non-normalized reflectance data is shown in Figs. 7(a), 7(c), and 7(d). H&E stained cross sectional photomicrographs are shown in Fig. 8 for the three tissues measured in Fig. 7. The differences in the three spectra reflect the differences in the tissue histology shown in Fig. 8. The lower reflectance observed in the spectra obtained from the denuded and irregularly keratinized samples, shown in Figs. 7(c) and 7(d), compared to spectra obtained from normal tissue, as shown in Fig. 7(a), may correlate to the degradation of the epithelial layer of the esophageal tissue sample evident in the tissue histology in Figs. 8(b) and 8(c). Degradation of the upper epithelial layer (mucosa), progressively through Figs. 7(a), 7(c), 7(d), likely reduces scattering and increases the submucosal sampling of the light, where the absorption is higher than in the mucosal region. Further exploration of the absorption and scattering coefficients for these types of tissues would enable classification algorithms to be utilized for diagnostic purposes.

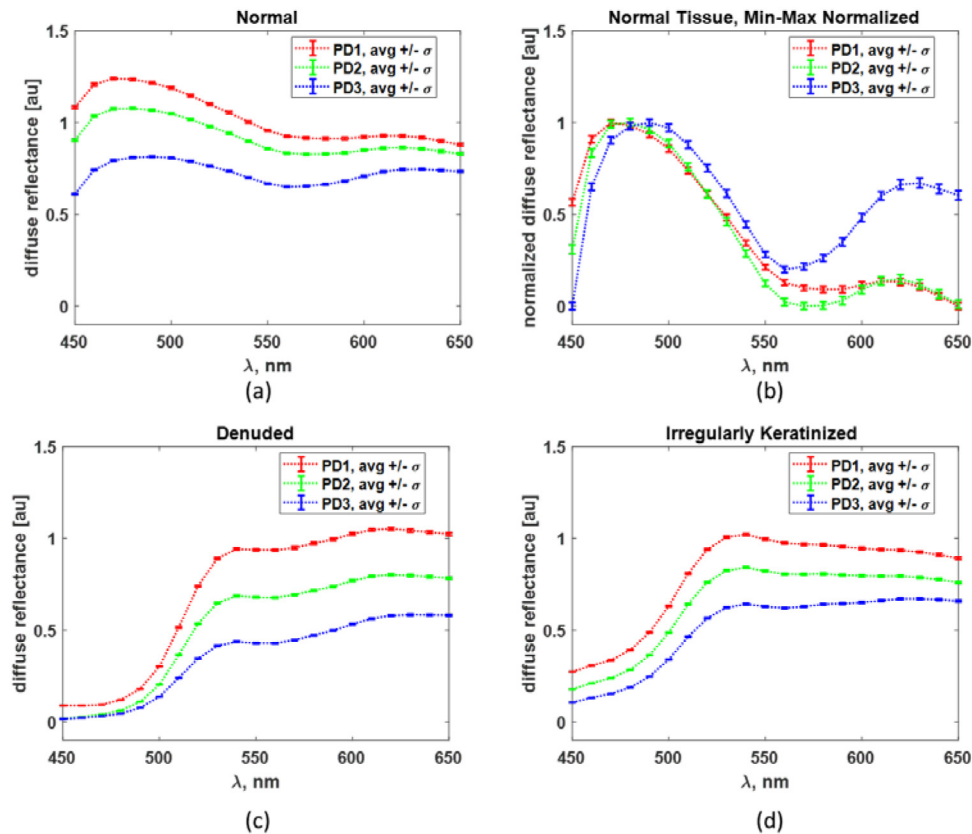


Fig. 7. Representative spectra for ex-vivo porcine esophagus. (a) normal, (b) min-max normalized normal, (c) denuded porcine, and (d) irregularly keratinized samples for which histology cross sections are shown in Fig. 8.

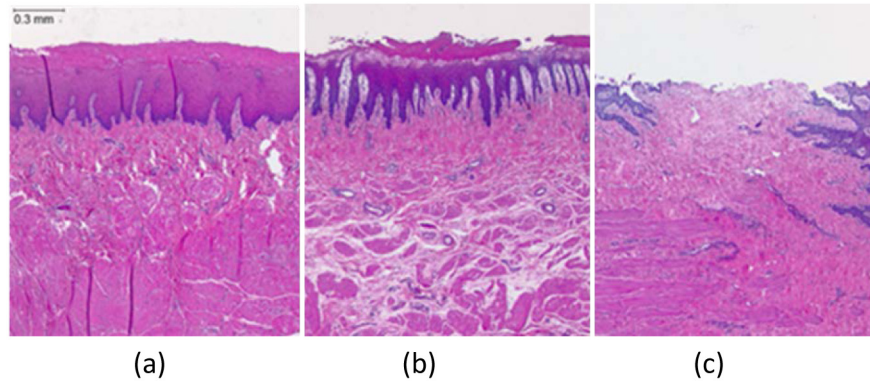


Fig. 8. Photomicrographs (4x mag) of H&E stained porcine (a) normal, (b) irregularly keratinized, and (c) denuded esophagus samples. The scale bar in the upper left of (a) is 300 μm long.

6. Summary and conclusions

The design, fabrication, and characterization of the first Si thin film multi-spectral SRDRS device targeting endoscopic applications is described herein. The MEOS probe was designed using a MC model informed by published colon absorption and scattering coefficients to achieve high contrast between normal and adenomatous colon tissue. The probe was optimized for an endoscopic format and high SNR across the relevant optical properties and wavelength range. Liquid phantoms representative of normal and adenomatous tissues were measured with the probe, and the MC model used in the design was validated by comparing the modeled MEOS reflectance output to the experimentally measured phantom reflectance. The prototype MEOS probe met all of the design criteria, including measured SNR above the target of 40 dB across all PDs for all phantom measurements. Exploratory measurements of porcine esophageal tissues were also performed, demonstrating that the MEOS device can achieve repeatable results in a realistic tissue environment, and indicated a change in the reflectance spectra with tissue histologic differences and the sensitivity to changes in tissue as a function of depth into the tissue.

Acknowledgements

The authors would like to thank City Packing, in particular Thomas McGarity and Jamie Corbett, for their generous contributions of porcine esophagus. This work was performed in part at the Duke University Shared Materials Instrumentation Facility (SMIF), a member of the North Carolina Research Triangle Nanotechnology Network (RTNN), which is supported by the National Science Foundation (Grant ECCS-1542015) as part of the National Nanotechnology Coordinated Infrastructure (NNCI). The authors would like to thank the staff of the Duke University SMIF for their technical assistance.

Disclosures

The authors declare that there are no conflicts of interest related to this article.